Monthly Notices of the ROYAL ASTRONOMICAL SOCIETY

MNRAS **535,** 406–418 (2024) https://doi.org/10.1093/mnras/stae2374
Advance Access publication 2024 October 17

On the nature of the eccentric eclipsing binary star SY Phe with a pulsating γ Dor component

Ahmet Erdem ,[1,2]★ Derya Sürgit,[1,3]★ Chris A. Engelbrecht,[4] Petr Zasche,[5] Volkan Bakış [6] and Fred Marang[4]

[1]Astrophysics Research Center and Ulupınar Observatory, Çanakkale Onsekiz Mart University, TR-17100 Çanakkale, Türkiye
[2]Department of Physics, Faculty of Science, Çanakkale Onsekiz Mart University, Terzioğlu Kampüsü, TR-17100 Çanakkale, Türkiye
[3]Department of Space Sciences and Technologies, Faculty of Science, Çanakkale Onsekiz Mart University, Terzioğlu Kampüsü, TR-17100 Çanakkale, Türkiye
[4]Department of Physics, University of Johannesburg, PO Box 524, Auckland Park 2006, South Africa
[5]Astronomical Institute, Faculty of Mathematics and Physics, Charles University Prague, CZ-180 00, Praha 8, V Holešovičkách 2, Czech Republic
[6]Department of Space Sciences and Technologies, Faculty of Science, Akdeniz University, Antalya 07058, Türkiye

Accepted 2024 October 11. Received 2024 October 11; in original form 2023 August 10

ABSTRACT

Spectroscopic observations of the eccentric binary system SY Phe were made at the South African Astronomical Observatory in 2019, 2020, and 2021, and its mid-resolution spectra were obtained. The radial velocities of the component stars were measured using the cross-correlation method and Fourier disentangling of the spectra. The spectral type (hence the effective temperature) of the primary star was determined from a model-atmosphere analysis. The radial velocity and *Transiting Exoplanet Survey Satellite* (*TESS*) light curves of the system were analysed, and its absolute parameters were derived. A strong (5.2 mmag) periodic signal with a frequency typical of γ Dor stars (1.169 cycles per day) dominates the Fourier spectrum of the light curve between the eclipses. Apsidal motion parameters of SY Phe were calculated by studying eclipse timing variations. The Geneva evolution models indicate an evolutionary age of 2 Gyr and solar metallicity for the primary component; however, although the position of the secondary component in the H–R diagram matches the isochrone of 2 Gyr, it appears to have a larger radius and higher effective temperature than expected for its determined mass. Here, the secondary component has too large a radius, which is in accordance with the radius discrepancy problem that has been encountered in other studies, especially in late-type dwarfs, and has not been solved for half a century.

Key words: binaries: eclipsing – stars: fundamental parameters – stars: individual: SY Phe – stars: oscillations – stars: variables: Gamma Doradus.

1 INTRODUCTION

The analysis of spectroscopic and photometric data of eccentric eclipsing binary (EB) systems facilitates the derivation of physical parameters of the component stars and their orbits with high precision. Observational data provide stringent tests and enable refinements of current theories of stellar structure and evolution. In this paper, a challenging eccentric EB star, SY Phe, is studied in detail for the first time.

SY Phe (=HD 9283, RA 01 30 30.84, DE −42 42 24.85, $V = 10.07$ mag) was discovered as a variable star by Hoffmeister (1949). Later, Hoffmeister (1958) classified SY Phe as an Algol-type binary system and discussed its additional / different light variations. The spectral type of the system was assigned as F8 by Spencer & Jackson (1936), as F4 by Hoffmeister (1949), and as F3/F5V by Houk (1978).

Despite its brightness, SY Phe has not been the subject of many studies. The only study analysing the system's light curve together with a number of period variations was reported by Zasche (2012), who derived preliminary physical parameters of the components based on WASP photometry (Pollacco et al. 2006). However, the value of the eccentricity was very uncertain, given the available data at that time. Kim et al. (2018) also examined the apsidal motion in the system by performing $O - C$ analyses of the times of minima. Most of the other literature sources on SY Phe consist of catalogues. For example, among the most recent catalogues, the Gaia DR3 catalogue of eclipsing-binary candidates (Mowlavi et al. 2023) includes SY Phe as an EB. Hence, a new study with more precise updated data would facilitate a better understanding of this system.

The SY Phe system contains an additional component detected interferometrically at a separation of about 4″ (Mason et al. 2001); however, no obvious movement on the mutual orbit is visible. Consequently, we can only speculate that the period associated with the additional component is probably very long. The Multiple Star Catalogue MSC (Tokovinin 2018) gives an estimate of >20 kyr.

2 SPECTROSCOPY

Spectroscopic observations of SY Phe were made at the South African Astronomical Observatory (SAAO). The 1.9-m telescope at the SAAO, equipped with the SpUpNIC (Spectrograph Upgrade:

★ E-mail: aerdem@comu.edu.tr (AE); dsurgit@comu.edu.tr (DS)

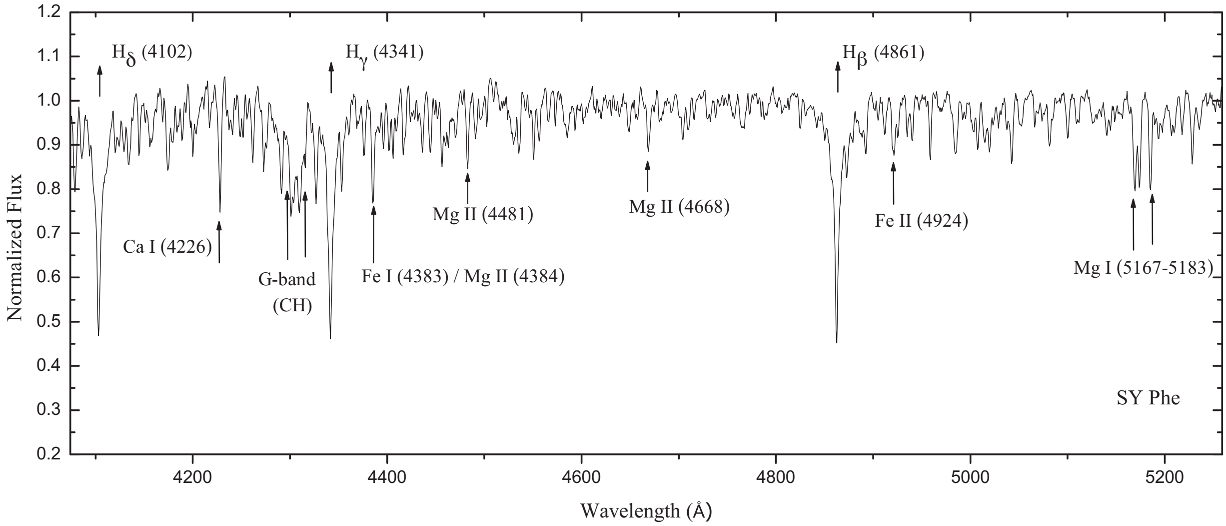

Figure 1. Sample spectrum of SY Phe observed at the orbital phase ∼ 0.5 in this study. Hydrogen Balmer lines and many metallic lines are marked in the spectrum.

Newly Improved Cassegrain; see Crause et al. (2016, 2019) for details) instrument, was used. A grating of the spectrograph which has 1200 lines/mm, a wavelength coverage of 400–525 nm, a blaze peak at 510 nm, and a resolution of 0.062 nm/pixel (corresponding to an approximate resolving power $R \gtrsim 3000$) was selected. A slit width of 1.35 arcsec was used for all spectroscopic observations of the EB system and associated radial velocity (RV) standard stars.

A total of 57 spectra were obtained for SY Phe across the 2019, 2020, and 2021 observing seasons. HR 3383 (A0V, $V_r = 6.21$ km s^{-1}), HD 693 (F8V, $V_r = 14.92$ km s^{-1}), and HR 6031 (A1V, $V_r = -8.65$ km s^{-1}) were observed contemporaneously as standard stars for RV measurements of the binary system. The exposure times varied within the range of 600–1200 s, depending on the weather conditions. Arc spectra using a Cu/Ar lamp were taken for wavelength calibration reasons before and after each stellar image. A set of quartz-iodine lamp images was also taken every night for flat-field calibrations. Standard IRAF procedures were used for spectral data reduction and calibrations.

An example of the observed spectra for SY Phe is shown in Fig. 1. The sample spectrum in this figure was selected from the conjunction phase of the components, with the more massive component transiting in front of the less massive component (i.e. at the orbital phase 0.5). The characteristic lines of middle F-type stars are seen in the spectrum of SY Phe.

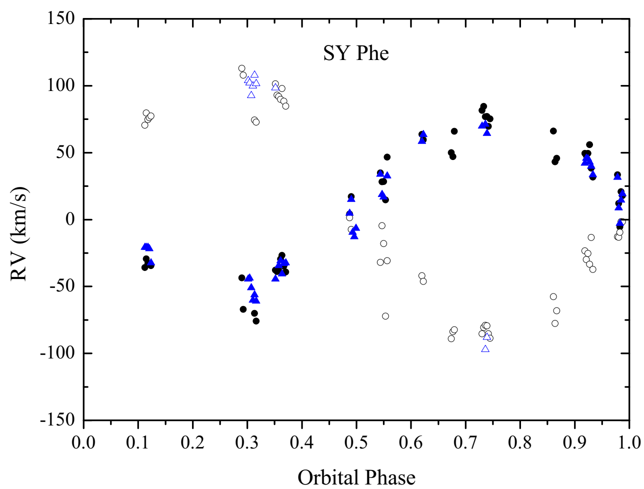

Figure 2. KOREL and cross-correlation RVs for SY Phe. Black circles denote KOREL RVs from H β lines, whereas blue triangles denote cross-correlation RVs from the metallic lines in the spectral regions of 4360–4800 Å and 5120–5230 Å. RVs of the primary and the secondary components are marked as filled and hollow symbols, respectively. To facilitate comparison, the KOREL RVs are shifted upwards by $V_0 = 10.24$ km s^{-1} calculated from the cross-correlation measurements since the KOREL code does not give the centre-of-mass velocity V_0 of the system. Orbital phases were calculated using the ephemerides given in Table 5.

2.1 Radial velocities

Two methods were used to measure the RVs of the components of SY Phe: cross-correlation and Fourier disentangling.

The cross-correlation measurements of RVs were performed with the IRAF package FXCOR which is based on the method of Tonry & Davis (1979) and Popper & Jeong (1994). The spectral range from 4360 to 4800 Å containing Mg II (4384, 4481, and 4668) and Fe I (4383) lines, and another spectral range from 5120 to 5230 Å containing Mg I triplet lines (5167–5183) (see Fig. 1) were selected for the RV calculations. The spectra of HD 693 was used as a template for deriving RVs of the binary components. The RVs derived from cross-correlation (and those obtained with KOREL) are shown in Fig. 2.

For separating the spectra of the component stars and for measuring their RVs, the KOREL Fourier disentangling code (Hadrava 1995) was applied. The spectral region around the Balmer line H β was disentangled in 48 of the observed spectra of SY Phe. Ten of the disentangled line-profiles of the H β line are shown in Fig. 3 to demonstrate the effectiveness of the code, in lieu of presenting the KOREL results for all 48 of the observed spectra. The blue lines in the upper part of this figure are the observed spectra at successive orbital phases from the top downward. Each observed spectrum was fitted by the superposition of disentangled profiles with RVs optimized by KOREL, and the corresponding fit is drawn in red. The RVs found from this solution are listed in Table A1 of Appendix A. These KOREL

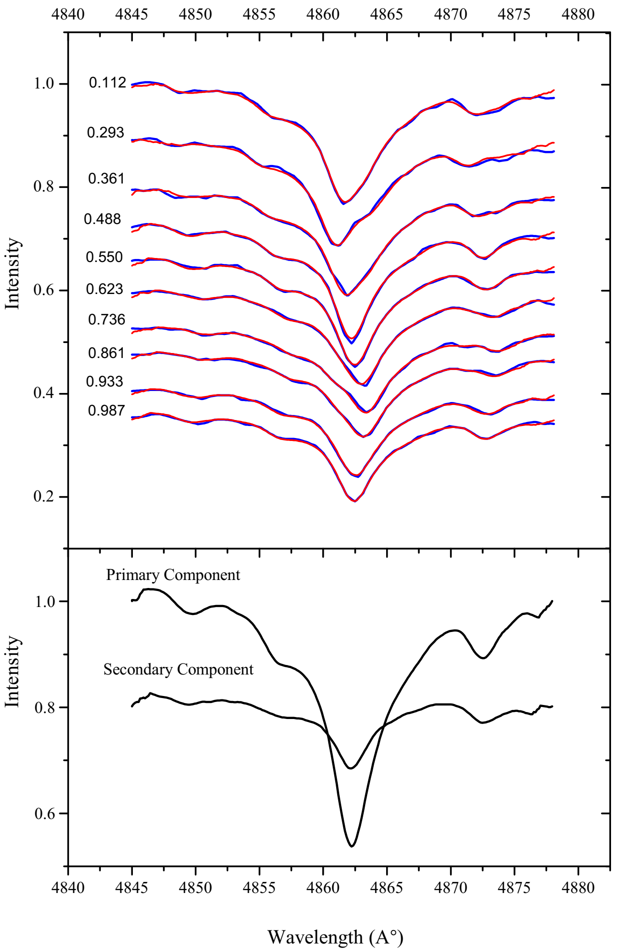

Figure 3. 10 sample disentangled line-profiles of the H β line in SAAO spectra of SY Phe. Blue line profiles in the upper part show the observed line profiles for successive orbital phases. The numbers at the beginning of the profiles indicate the orbital phases. They are overplotted by red line profiles representing their reconstructions from the disentangled profiles, which are displayed by two black line profiles in the bottom part. Here, the intensity is given in units of the continuum level and the wavelength is in Å.

RVs, together with the cross-correlation RVs, are also shown in Fig. 2.

As can be seen from Fig. 2, KOREL RVs were preferred for the RV analysis of SY Phe, especially because a much larger number of RVs of the secondary component can be measured with the KOREL code. The program JKTEBOP (Southworth 2013, 2023) was then applied to derive orbital parameters of SY Phe, using the measured KOREL RVs of the components. During the iterations, the orbital period (P) of the binary system was fixed at the value listed in Table 5 in Section 6. The RV semi-amplitudes (K_1 and K_2) of the components, and the eccentricity (e), periastron longitude (ω), and time of primary eclipse (T_0) of the system were taken as the free/adjusted parameters. Final orbital parameters of SY Phe, together with their errors, are listed in Table 1. Throughout the text, we follow a consistent notation for the primary and secondary components, respectively. The primary component is denoted by a '1', and the secondary component by a '2', for all the parameters, where the primary component is the star eclipsed at phase 0.0. The comparison of the RVs of SY Phe with the JKTEBOP model fitting is also shown in Fig. 4.

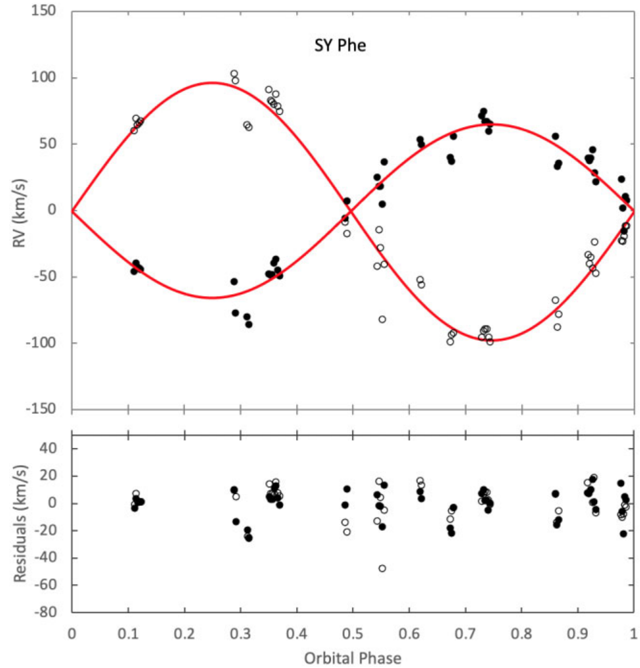

Figure 4. KOREL RVs from H β lines with the JKTEBOP model fitting. Residuals to the RV model are plotted in the bottom figure.

Table 1. Orbital parameters of SY Phe from KOREL RVs.

Parameter	Value
P (d)	5.270891 (fixed)
T_0 (HJD)	2454163.2742 ± 0.0064
e	0.0066 ± 0.0015
ω (deg)	212 ± 16
K_1 (km s^{-1})	65.37 ± 2.20
K_2 (km s^{-1})	97.02 ± 2.66
Derived parameters	
$a_1 \sin i$ (R$_\odot$)	6.81 ± 0.23
$a_2 \sin i$ (R$_\odot$)	10.10 ± 0.28
$M_1 \sin^3 i$ (M$_\odot$)	1.40 ± 0.06
$M_2 \sin^3 i$ (M$_\odot$)	0.94 ± 0.04
$q = M_2/M_1$	0.67 ± 0.03
rms RV$_1$ (km s^{-1})	10.4
rms RV$_2$ (km s^{-1})	12.6

Note: rms is the root mean square of the residuals from the best-fitting model.

3 *TESS* PHOTOMETRY

SY Phe was observed by *TESS* (*Transiting Exoplanet Survey Satellite*) with a 30-min cadence in Sector 02 (August 23 to September 20, 2018), with a 30-min cadence in Sector 03 (September 20 to October 17, 2018), with a 10-min cadence in Sector 29 (August 26 to September 21, 2020), with a 10-min cadence in Sector 30 (September 23 to October 20, 2020), and with a 200-s cadence in Sector 69 (August 25 to September 20, 2023). We downloaded the *TESS* data from the Mikulski Archive for Space Telescopes (MAST) archive[1] and extracted the Simple Aperture Photometry (SAP) and the Pre-

[1] https://mast.stsci.edu/portal/Mashup/Clients/Mast/Portal.html

Table 2. The fitted parameters of SY Phe for each of the six *TESS* half-sector light curves using the WD code. The uncertainties are derived from WD + Monte Carlo method.

Parameter	Sector 29-1	Sector 29-2	Sector 30-1	Sector 30-2	Sector 69-1	Sector 69-2
e	0.0082 ± 0.0005	0.0059 ± 0.0006	0.0056 ± 0.0004	0.0057 ± 0.0004	0.0095 ± 0.0004	0.0076 ± 0.0004
ω (deg)	230 ± 20	191 ± 20	188 ± 20	191 ± 18	234 ± 15	214 ± 16
$\Delta\phi$	-0.0006 ± 0.0001	-0.0008 ± 0.0001	-0.0005 ± 0.0001	-0.0008 ± 0.0001	-0.0009 ± 0.0001	-0.0006 ± 0.0001
i (deg)	88.67 ± 0.20	88.50 ± 0.22	88.50 ± 0.21	88.47 ± 0.18	88.47 ± 0.16	88.46 ± 0.16
T_1 (K)	6600 (fixed)	6600 (fixed)	6600 (fixed)	6600 (fixed)	6600 (fixed)	6600 (fixed)
T_2 (K)	6138 ± 18	6142 ± 22	6184 ± 26	6170 ± 19	6124 ± 13	6109 ± 13
$q = M_2/M_1$	0.67 (fixed)	0.67 (fixed)	0.67 (fixed)	0.67 (fixed)	0.67 (fixed)	0.67 (fixed)
Ω_1	11.2926 ± 0.0919	11.3787 ± 0.1263	11.2984 ± 0.1011	11.2773 ± 0.0985	11.3600 ± 0.0836	11.3730 ± 0.0883
Ω_2	11.1423 ± 0.1581	11.4758 ± 0.1956	11.4304 ± 0.1599	11.3462 ± 0.1400	11.4612 ± 0.1253	11.4582 ± 0.1227
r_1 (mean)	0.094 ± 0.005	0.093 ± 0.006	0.094 ± 0.006	0.094 ± 0.006	0.094 ± 0.006	0.093 ± 0.006
r_2 (mean)	0.067 ± 0.005	0.065 ± 0.006	0.065 ± 0.006	0.066 ± 0.006	0.065 ± 0.006	0.065 ± 0.006
L_1	0.55 ± 0.02	0.57 ± 0.03	0.57 ± 0.02	0.57 ± 0.02	0.57 ± 0.02	0.57 ± 0.02
L_2	0.24 ± 0.02	0.23 ± 0.03	0.22 ± 0.02	0.23 ± 0.02	0.23 ± 0.02	0.23 ± 0.02
L_3	0.21 ± 0.02	0.20 ± 0.03	0.21 ± 0.02	0.20 ± 0.02	0.20 ± 0.02	0.20 ± 0.02
χ^2_{red} (LC)	1.00	1.00	1.00	1.00	1.00	1.00
ν (LC)	1392	1354	1627	1640	4095	4355
Δl (LC)	0.001155	0.000745	0.001195	0.00096	0.00092	0.0013

Table 3. Adopted LC parameters of SY Phe derived from the six *TESS* half-sector light curves fitted with the WD code. Here, the weighted mean and weighted standard errors of the LC parameter values given in Table 2 are presented.

Parameter	Value
e	0.0071 ± 0.0015
ω (deg)	211 ± 19
i (deg)	88.50 ± 0.07
T_1 (K)	6600 (fixed)
T_2 (K)	6134 ± 24
$q = M_2/M_1$	0.67 (fixed)
r_1 (mean)	0.094 ± 0.005
r_2 (mean)	0.066 ± 0.006
L_1	0.57 ± 0.02
L_2	0.23 ± 0.01
L_3	0.20 ± 0.01

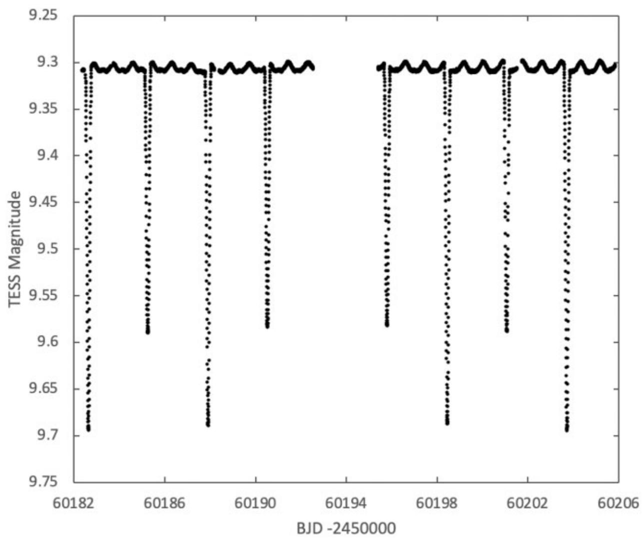

Figure 5. Sector 69 (with a 200-s cadence) *TESS* photometry of SY Phe.

search Data Conditioning Simple Aperture Photometry (PDCSAP) from the FITS files (Jenkins et al. 2016). We preferred to use the SAP data because there is some scatter in the PDCSAP data, and it is about 0.10 mag deeper in the minima than the SAP data. We then selected the SAP data with a quality flag of zero and used approximately 15 000 points from all sectors. On the other hand, in the SAP data in all sectors, the CROWDSAP parameter, which is the ratio of the target flux to the total flux in the photometric aperture, is given around 0.80. This value shows that only approximately 20 per cent of the observed flux in the SAP aperture does not come from the target. Therefore, in the light curve (LC) analysis, we entered the input value of the third light contribution parameter (L_3) as 0.20. In the LC analysis results, L_3 was indeed obtained as 0.20 ± 0.01 (see Tables 2 and 3).

The *TESS* Sector 69 photometric data is shown in Fig. 5 as an example. It is clearly seen in these *TESS* light curves that SY Phe exhibits oscillations with small amplitudes, especially in the maximum levels. Because Sectors 02 and 03 had a 30-min cadence, we only used the light curve from Sectors 29 and 30 (with a 10-min cadence) and Sector 69 (with a 200-s cadence) for the pulsation analysis, to ensure that a reasonably high Nyquist frequency could be sustained for the analysis.

First, we followed a procedure similar to that of Maceroni et al. (2013, 2014), to find the EB model parameters more accurately: (i) pre-whitening the original *TESS* light curve (denoted as LCO hereafter) using the strongest frequencies (that is, 1.169 d^{-1} and 2.333 d^{-1}) obtained from the harmonic fit computed outside eclipses, and (ii) analysing the light curves with the majority of the pulsation signal having been removed.

The resulting *TESS* light curves (denoted as LCEB hereafter) of SY Phe, as residuals of the harmonic fit, is shown in Fig. 6. These light curves are phased with the linear ephemeris given in Table 5.

4 ANALYSIS

For the analysis of the *TESS* LCEBs, the numerical integration method (WD) of Wilson & Devinney (1971) was applied. This

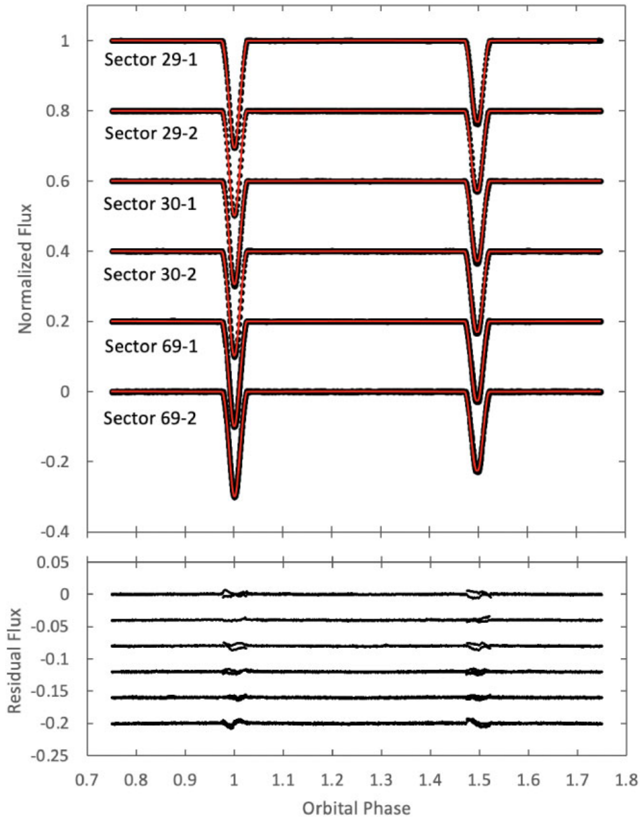

Figure 6. Six *TESS* half-sector light curves with the WD model fitting. Residuals to the LC model are plotted in the bottom figure and are arranged in the order shown in the top figure, with residuals after those of Sector 29-1 shifted downwards.

method models the light curve of a given binary star, considering mainly the ellipticity and proximity effects, and the equipotential surfaces of the components. In the literature, it is widely believed that the formal errors for the free / adjusted parameters given by the WD program in iterations are generally underestimates (e.g. Maxted et al. 2020). Therefore, in order to find more reliable error estimates, we followed a procedure similar to that of Overall & Southworth (2024): the data obtained in each 13.7 d orbit (half-sector) of the three *TESS* sectors was analysed independently and the mean value and standard error calculation for each adjusted parameter were made from the six independent measurements. In addition, the program WD, combined with the Monte Carlo (MC) optimization procedure discussed by Zola et al. (2004), was used to give the input values and errors of the adjusted parameters for each half-sector data analysis.

Four different methods were used to determine the spectral type and, thereby, the effective temperature of the primary component of SY Phe. (i) For the spectral type of the system, the range of F3 to F8 given in the literature was considered. Then, the observed spectra of the system at phases close to the conjunction of the components were studied. Using the line matching method for the H γ, H β, Ca I (4226), Fe I (4383), Fe II (4924), Mg II (4384, 4481, 4668), and Mg I (5167–5183) triplet lines, and using the (CH) *G* band (see Fig. 1) in the spectra observed at the conjunction phases, and sample spectra for F-type main-sequence stars given in Gray & Corbally (2008), the spectral type of the system was estimated to be close to F5V. (ii) The solution of the RV curves obtained in the present study corresponds to a mass of the primary component of approximately 1.4 $M_{\odot}$, which is in agreement with a spectral type of F5V. (iii) The colour index of $B - V = 0.42 \pm 0.04$, which was derived from the Fabricius et al. (2002) study, indicates that the spectral type of the system is close to F4/5. (iv) The fact that the orbital inclination is close to 90 degrees and the primary component is larger in size than the secondary component in the trial solutions implies that no light is seen from the secondary and we see only the light from the primary component in the spectra observed at phase ∼0.5 (spectrum 40 in Table A1). Thus, the atmospheric parameters of the primary component could be obtained from the spectrum at phase 0.5. Nevertheless, since our spectral data are of medium resolution, we adopted log *g* from simultaneous light and RV solutions, while metallicity and microturbulence velocity parameters were adopted to be solar values under LTE conditions. A grid of ATLAS9 (Castelli & Kurucz 2003) model atmospheres was calculated for a range of temperatures (ΔT =5500–7000 K, δT =50 K), rotational velocities ($\Delta V_{\rm rot}\sin i$ = 100–140 km s^{-1}, $\delta V_{\rm rot}\sin i = 20$ km s^{-1}), and metallicities ($\Delta[M/H]$ =–0.3–0.3 K, $\delta[M/H] = 0.1$ dex), and the observed spectrum at the secondary minimum was fitted with the synthetic spectra under the χ^2-minimization scheme. In the bottom panel of Fig. 7, the χ^2 distribution among the temperatures and metallicity parameters is shown. Among the models, two spectra (with $T = 6600$ K, $V_{\rm rot}\sin i = 120$ km s^{-1}, and $[M/H] = 0.0$ and $T = 6450$ K, $V_{\rm rot}\sin i = 120$ km s^{-1}, and $[M/H] = -0.1$, respectively) appear to fit the observed spectrum with the lowest χ^2. Although the values of χ^2 for these two models are close to each other ($\chi^2_{[M/H]=0.0} = 0.001266$ and $\chi^2_{[M/H]=-0.1} = 0.001269$), the model with solar metallicity was accepted since the value of $T_1 = 6600$ K agrees with the spectral type of the primary component assigned as F4/5V from the three methods mentioned above. Thus, the effective temperature of the primary component, which has a larger mass according to the RV curve solution, was adopted as 6600 K and this value was fixed. The effective temperature of the secondary component was adjusted in the WD iterations.

On the other hand, due to the relatively low resolution of the SAAO spectra, the rapid rotation of the primary component given by the stellar LTE atmosphere modelling will be left as a possibility that needs to be checked with high resolution spectra. Therefore, we assumed a pseudo synchronization of rotation at periastron in the WD iterations.

Other parameters that were allowed to be adjusted in the WD iterations included: the eccentricity (e), longitude of the periastron (ω), and orbital inclination (i) of the binary system, phase shift (which is to allow the WD code to adjust for a zero point error in the ephemeris used to compute the phases; the unit is the orbital period, $\Delta\phi$), non-dimensional surface potential parameter of each component (Ω_1, Ω_2), fractional luminosity of the primary component (L_1), and third light contribution (L_3).

The mass ratio of the system ($q = M_2/M_1$) was taken as constant at the value of spectral mass ratio ($q = 0.67$) found from the JKTEBOP solution of the RV curves in Section 2.1. A quadratic limb-darkening law was assumed; the limb-darkening coefficients of the components were taken from Claret (2017). The bolometric gravity darkening exponents were adopted from Lucy (1967) to be 0.32 for convective atmospheres of the components ($T < 7200$ K). The bolometric albedos of the components were set to 0.5 for convective atmospheres, following Ruciński (1969). These parameters were kept constant during all iterations.

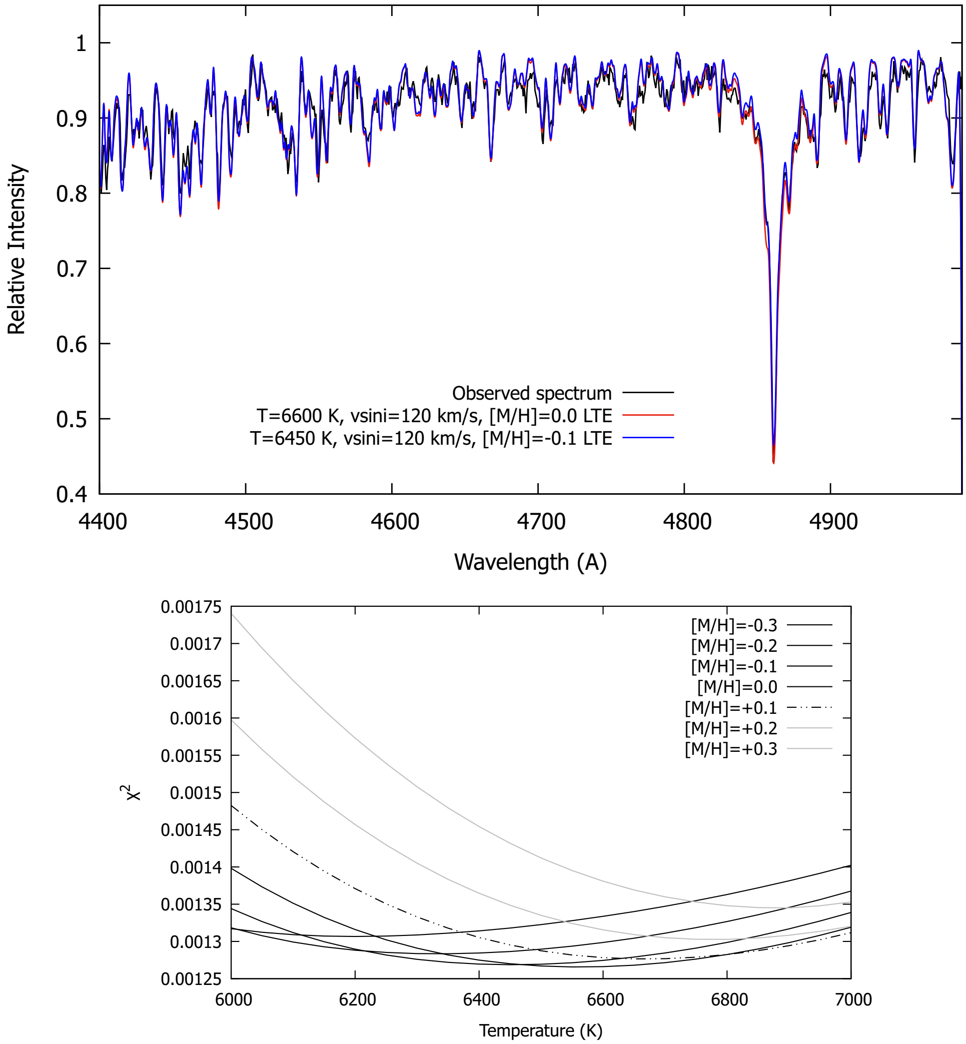

Figure 7. *Top:* two LTE synthetic spectra together with the observed spectrum of SY Phe at orbital phase $\phi \sim 0.5$ where the secondary is totally eclipsed. *Bottom:* the χ^2 distribution for the grid of synthetic spectra. The synthetic spectra on the top panel are the two best-fitting models.

The final model values derived from the six *TESS* half-sector LCEBs of SY Phe are listed in Table 2. The values of χ^2 were obtained from $\sum_i (l_{i,o} - l_{i,c})^2/\Delta l_i^2$ (Bevington 1969), where $l_{i,o}$ and $l_{i,c}$ are the observed and calculated light levels at a given phase, respectively, and Δl_i is an error estimate for the measured values of $l_{i,o}$. The reduced χ-squared value was obtained from $\chi^2_{\rm red} = \chi^2/\nu$, where ν is the number of degrees of freedom of the data set, that is, $\nu = N_{\rm obs} - N_{\rm param}$, where $N_{\rm obs}$ is the number of observations and $N_{\rm param}$ is the number of parameters in the model. The adopted LC parameters for SY Phe are given in Table 3; these are the weighted mean and standard errors of the corresponding fitted parameters across the six *TESS* half-sectors.

The comparison of the *TESS* half-sector LCEBs of SY Phe with the results generated by the WD models are shown in Fig. 6. Here, quite a large scatter is noticeable in the residual light curves around the minimum / eclipse phases. A similar case is seen in the studies of Maceroni et al. (2014) on KIC 3858884 and Southworth (2022) on ZZ UMa. Maceroni et al. (2014) explained this scatter as depending on the stellar surface representation in PHOEBE (and WD), in which the aligned border of the first tile of each meridian produces a seam along the central line facing the companion star. Southworth (2022) attributed this scatter to the effect of the starspots appearing on the surfaces of both components on the surface-brightness ratio of the system.

The spectral energy distribution (SED) data of SY Phe in the Simbad archive (Wenger et al. 2000) were analysed as a further check on the temperature and radius of the components obtained from the simultaneous RV + LC solution. In this analysis, the method described by Bakış & Eker (2022), who studied 209 double-lined detached EBs to determine their multiband bolometric corrections, was used. The temperatures and radii of the components were taken from Table 6, whereas the distance was adopted from the GAIA DR3 catalogue (Gaia Collaboration 2022). In Fig. 8, the SED model with $E(B-V) = 0.04 \pm 0.01$ mag optimally represents the SED data of SY Phe with the parameters (T_1, T_2, R_1, and R_2) derived in this study. The crosses shown in Fig. 8 indicate data at least 3σ away from the model fit. These data were not used in the χ^2 calculation and, therefore, were not considered when finding the best-fitting model for SY Phe. These measurements ($\geq 3\sigma$) are from 2MASS (Skrutskie et al. 2006), CTIO/DECam (Abbott et al. 2021) and VHS (McMahon et al. 2013) and are associated with a very faint ($\sim 19^m$ in 2MASS *J* band) object

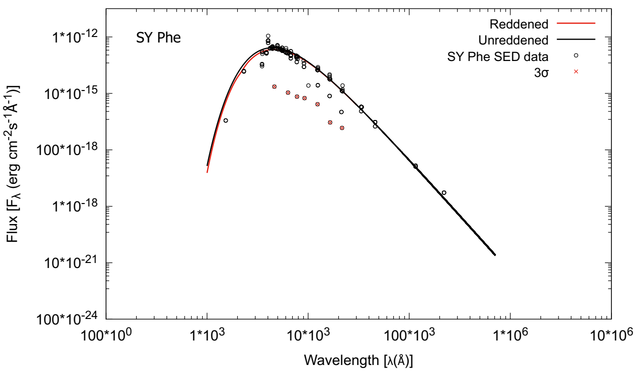

Figure 8. SED data and model for SY Phe. The SED data refers to a region within 1 arcsec around SY Phe.

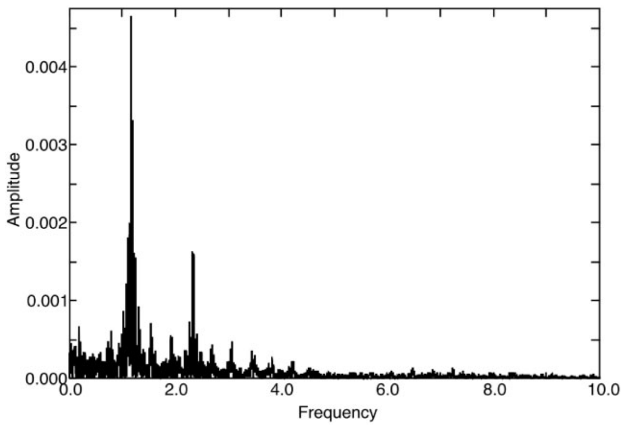

Figure 9. Amplitude spectrum of the *TESS* sector 29-30-69 light curves for SY Phe, after subtraction of the WD binary model (excluding eclipses). The amplitude is in mmag on the vertical axis and the frequency is in cycles d^{-1} on the horizontal axis.

identified as a galaxy with probability ≥0.9 (McMahon et al. 2013).

5 PULSATION ANALYSIS

We performed a time series analysis of the *TESS* light curve of SY Phe obtained in sectors 29, 30, and 69, after subtracting the orbital light curve solution to obtain a residual light curve. As explained in Section 3, the original light curve was prewhitened by the strongest two periodic signals (excluding the orbital signal) in the light curve before the orbital light curve solution was obtained. The orbital light curve solution was then subtracted from the original light curve to obtain the residual light curve. This procedure resulted in a much cleaner (less noisy) residual light curve for the pulsation analysis. We also removed the eclipse phases from the residual light curve before proceeding with the pulsation analysis, to avoid undue interference. Two very strong periodic signals dominate the amplitude spectrum of the residual light curve, displayed in Fig. 9. The primary peak (with a light amplitude of 5.2 mmag) lies at a frequency of 1.169 cycles per day. Given the temperature, mass and radius of the primary component of the system that we have derived from the orbital analysis, this strong periodabove. We see no other physical cauic signal is most likely the signature of a γ Dor pulsation mode. The secondary strong peak (with an amplitude of 2.1 mmag) in

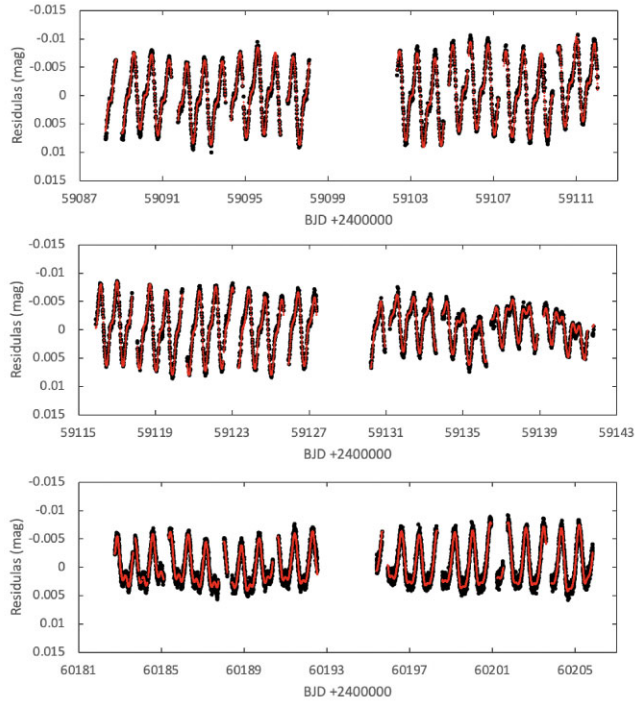

Figure 10. Residual points of *TESS* Sector 29 data (upper panel), Sector 30 data (middle panel), and Sector 69 data (lower panel) after LC model and final fits (red points) obtained from the frequency analysis in Section 5.

the periodogram lies at 2.333 cycles per day, at exactly twice the primary frequency. The most plausible interpretation of this second peak is that it is the second Fourier harmonic associated with the primary frequency, originating from the pulsation not being perfectly sinusoidal in the light curve. This hypothesis is supported by the fact that the third and fourth harmonics of the primary frequency were also detected at significant signal-to-noise levels. Indeed, a departure of the proposed γ Dor pulsation mode (signified by the peak at 1.169 cycles per day) from sinusoidal behaviour appears visible as a clear 'stillstand' feature seen in the residual light curve displayed in Fig. 10. The shape of this feature is reminiscent of features seen in the light curves of certain RR Lyrae and β Cephei pulsators (see, for example, Aerts et al. 1995 and Fokin et al. 2004). However, a puzzling observation is that the stillstand feature is only clearly visible in the residual light curves from *TESS* sectors 29 and 30. It is not clearly visible in the residual light curve from sector 69.

We used the PERIOD04 package (Lenz & Breger 2004) to obtain a detailed prewhitening sequence of the residual light curve. The standard prewhitening procedure applied in the PERIOD04 package consists of subtracting a simultaneous smallest-least-squares fit of a set of periodic signals from the original light curve. The residual light curve (obtained subsequent to the prewhitening process) is then sequentially analysed for further periodic signals. In theory, this approach avoids the 'skewing' of pulsation signals by other periodic effects, which could include orbital motion, data-sampling artefacts, and instrumental fluctuations. We also used PERIOD04 to calculate the local noise levels in the Fourier spectrum. The first fourteen frequencies obtained from the prewhitening sequence had amplitudes at least four times higher than the local noise levels in the Fourier spectrum.

Table 4. Results of periodogram analysis based on *TESS* Sectors 29, 30, and 69 data of SY Phe (13084 points spread across 1117 d).

Frequency No	Frequency (cycles/d)	Amplitude (mmag)	Phase
F1	1.169	5.15	0.5606
F2	2.333	2.12	0.1584
F3	1.180	1.19	0.0101
F4	0.186	0.87	0.8412
F5	2.348	0.69	0.8854
F6	1.151	0.65	0.3527
F7	0.034	0.50	0.3590
F8	0.384	0.40	0.0430
F9	0.086	0.38	0.9965
F10	0.155	0.38	0.9790
F11	1.197	0.36	0.7122
F12	3.497	0.19	0.7781
F13	0.343	0.19	0.9846
F14	4.675	0.11	0.5441

This threshold of four-times-local-noise is generally adopted to separate significant signals in a periodogram from signals that are not sufficiently strong to be considered significant. The fourteen significant frequencies thus identified are listed in Table 4, with their respective amplitudes and phases as identified through the prewhitening process.

Aside from the two frequency peaks in the Fourier spectrum already discussed above (denoted F1 and F2, respectively), the remaining periodic signals listed in Table 4 are (in order of prominence): F3 = 1.180 cycles per day (c/d) (=F1 + 0.012 c/d); F4 = 0.186 c/d (this is simply the signature of the orbital motion); F5 = 2.348 c/d (this corresponds exactly (to the fourth decimal point) to F1 + F3, so it is interpreted as an interference signal); F6 = 1.151 c/d (= F1 - 0.017 c/d); F7 = 0.034 c/d (corresponding closely to the length of each of sectors 29 and 30, so it is most likely a finite timespan effect); F8 = 0.384 c/d (close to 2 × F4); F9 = 0.0858 c/d (origin undetermined); F10 = 0.155 c/d (origin undetermined); F11 = 1.197 c/d (=F3 + 0.018 c/d = F1 + 0.029 c/d); F12 = 3.497 c/d (=3 × F1, thus the third harmonic associated with F1); F13 = 0.343 c/d (origin unknown); and F14 = 4.675 c/d (=4 × F1, thus the fourth harmonic associated with F1). The signal-to-local-noise ratio of F14 was 6.78, so it is regarded as a statistically significant signal. All subsequent peaks in the periodogram had ratios well below 4, and are thus regarded as not signifiant. F3, F6, and F11 appear to be subsidiary peaks separated from F1 by 0.012, 0.017, or 0.029 cycles per day. It is plausible to ascribe these small separations to the interference caused by the discontinuities in the dataspan. The length of sectors 29 and 30 together is a bit shorter than 55 d. The inverse of this is 0.018 cycles per day. The length of the sector 69 dataspan is 21.3 d. The inverse of this is 0.047 cycles per day. These numbers are of the same order of magnitude as the separations of the subsidiary peaks described above. We see no other physical cause to explain these numbers.

A Fourier fit of the results of our time series analysis to the residuals of the *TESS* light curves is shown in Fig. 10. We used the fourteen frequencies listed in Table 4, with their respective amplitudes and phases as identified through the prewhitening process, for the fit. The fit is clearly dominated by the strong signal corresponding to F1 (and its higher harmonics).

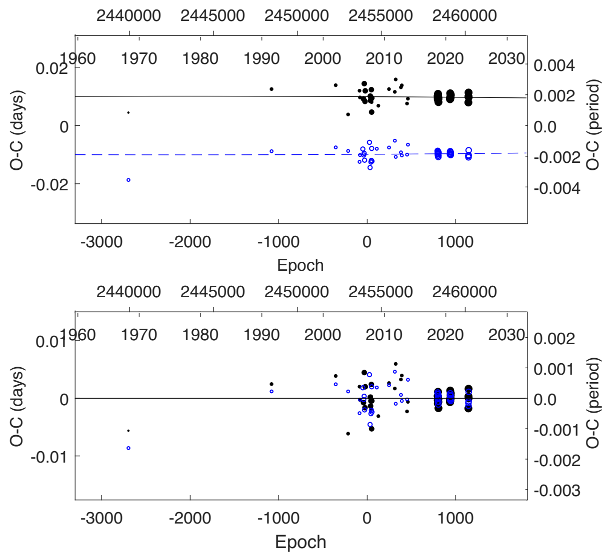

Figure 11. $O - C$ diagram of SY Phe and apsidal motion model fitting. Black points represent primary minima; blue open circles represent secondary minima. The sizes of the symbols are proportional to their weights. Residuals are shown in the lower panel.

Table 5. Apsidal motion parameters of SY Phe.

Parameter	Value
T_0 (HJD)	2454163.2678 ± 0.0020
P (d)	5.270891 ± 0.000013
e	0.006 ± 0.003
ω (deg)	192 ± 30
$\dot{\omega}$ (deg yr^{-1})	0.53 ± 0.19

6 APSIDAL MOTION

In order to trace any changes in the orbital period or detect the long-term evolution of the orbit – including the apsidal motion effect – we collected all available times of eclipses for the star. The system does not appear to have been the subject of a dedicated observing campaign before. The only available data are in data bases generated by automated ground-based telescopes and satellites. The majority of the extant data were used in Zasche (2012); however, several additional data points were derived for the current study. These consisted mainly of new times of eclipses from the *TESS* data and from the KELT survey (Pepper et al. 2007; Oelkers et al. 2018). All the times of eclipses used for the apsidal motion analysis are listed in Table B1 of Appendix B.

However, even when adding the new, precise data, no evolution of the ω angle and the rotation of the apsides (see Fig. 11) could be detected. These motions of the system's orbit are very slow, either at the edge of or well below the level of detectability with the current data set. Therefore, the solution as presented in Table 5is still rather formal, with very large uncertainties. Despite the system's large photometric amplitude, high brightness, and accessible period, the star was not observed frequently by older photographic surveys. The only digitized plates providing some magnitude estimates were those from the APPLAUSE archive (Groote et al. 2014). However, the rather scattered data do show only a few slightly dimmed points near the eclipses, and therefore any

Table 6. Absolute parameters of SY Phe.

Parameter	Primary	Secondary
a ($R_\odot$)	16.92 ± 0.32	
M ($M_\odot$)	1.41 ± 0.12	0.94 ± 0.12
R ($R_\odot$)	1.59 ± 0.10	1.13 ± 0.12
log g	4.18 ± 0.22	4.31 ± 0.20
T (K)	6600 ± 300	6068 ± 300
log L	0.64 ± 0.11	0.21 ± 0.12
M_{bol} (mag)	3.15 ± 0.28	4.21 ± 0.36
M_V (mag)	3.17 ± 0.28	4.25 ± 0.36
$E(B–V)$ (mag)	0.04 ± 0.01	
$B–V$ (mag)	0.42 ± 0.04[a]	
V (mag)	10.07 ± 0.02[a]	
$M_{\rm V}$ (system) (mag)	2.83 ± 0.40	
d (pc)	265 ± 36	

[a]Fabricius et al. (2002).

time-of-eclipse estimate is still rather questionable and affected by large uncertainties. These data from the 1960's only serve to confirm that the ω angle remains almost the same over this time interval. Any speculation about possible variations and a hypothetical third body would be premature due to the insufficient quality of these old data points. To conclude, we report an apsidal motion period of approximately 700 yr, but this number should be considered as a very rough estimate, or a lower limit only. With the current data set the solution is almost insensitive to different eccentricity values.

7 ABSOLUTE PARAMETERS

The absolute properties of the EB system SY Phe were derived using the parameters obtained from the solutions of the RV and light curves (see Tables 1 and 3) and the appropriate laws of physics. In the first step, the masses of the components (M_1, M_2) were calculated from Kepler's third law. The fractional radii of the components (r_1, r_2) from the LC solution and the semimajor axis of the binary system's relative orbit (a) from the RV solution were used to derive the absolute radii (R_1, R_2). In the second step, the surface gravitational accelerations (g_1, g_2) of the components were computed from the well-known formula ($g = GM/R^2$) using the masses and radii. In the third step, the bolometric magnitudes ($M_{\rm bol}$) and luminosities (L) of the component stars were calculated using the following two equations derived from Pogson's formula and the absolute radii and effective temperatures listed in Table 6:$M_{\rm bol} = M_{\rm bol,\odot} + 10\log {\rm T}_\odot - 10\log T - 5\log(R/{\rm R}_\odot)$, and $L/{\rm L}_\odot = 10^{0.4(M_{\rm bol,\odot}-M_{\rm bol})}$. The nominal solar values, which were adopted by IAU 2015 Resolutions B2 and B3, were used in our calculations. The absolute visual magnitudes $M_{\rm V}$ were derived from the bolometric correction formula, $BC = M_{\rm bol} - M_{\rm V}$. Bolometric corrections for the components were taken from the online version of the colour tabulation of Pecaut & Mamajek (2013), according to their effective temperatures.

In the final step, the distance to the system was calculated from the well-known adaptation of Pogson's law: $M_{\rm V} = m_{\rm V} + 5 - 5\log(d) - A_{\rm V}$. The colour excess for SY Phe was taken from the SED analysis in Section 4. Then, the interstellar absorption for the system was estimated as $A_{\rm V} = 3.1E(B{-}V)$.

The distance to SY Phe – including the correction for interstellar absorption – was computed as 265±36 pc, which matches the distances of 272 ± 2 and 264 ± 1 pc given by Gaia-DR2 (Gaia Collaboration 2018) and Gaia-DR3 (Gaia Collaboration 2022), respectively. The photometric parallax formulation of Budding & Demircan (2007) produces a distance of 288 ± 40 pc. This consistency among the distance values found with different formulas and methods shows the accuracy of the observationally determined absolute parameters of SY Phe.

The final absolute parameters of SY Phe as determined by our analysis, together with their errors, are listed in Table 6.

8 EVOLUTIONARY STATUS

Geneva (e.g. Yusof et al. 2022; Ekström et al. 2012) evolution models were used to study the evolutionary status of SY Phe. According to the measured parameters listed in Table 6, the Geneva evolutionary tracks for the components were created using the interpolation interface at the Geneva group webpage.[2] Since the model with solar metallicity was accepted from the model-atmosphere analysis in Section 4, the solar metallicity given as $Z = 0.014$ at the Geneva's webpage was adopted for SY Phe.

The H–R diagram displayed in the top panel in Fig. 12 was used for estimating the ages of the components. In this diagram, the positions of the two components are plotted on the evolutionary tracks for their measured masses. Accordingly, the isochrone of log(age) = 9.30 for $Z = 0.014$ matches the positions of both components. However, according to the H–R diagram, it is seen that the measured radius and temperature of the secondary component are considerably higher than the radius and temperature predicted in the model.

On the other hand, as discussed by Southworth & Clausen (2007), since the mass, radius, and temperature are quantities directly measured from observations, using mass versus radius and mass versus temperature diagrams is one of the best approaches to examine the evolutionary status of a given binary star. Therefore, in order to see more clearly whether the evolutionary age found from the H–R diagram fits the physical parameters of the components, the positions of the components and the isochrone of log(age) = 9.30 for $Z = 0.014$ were drawn on the mass versus radius and mass versus temperature diagrams (see the middle and bottom panels of Fig. 12). These two diagrams show that the isochrone of 2 Gyr for $Z = 0.014$ represents the physical properties of the primary component well, while the secondary component is approximately 0.25 $R_\odot$ (20 per cent) larger and 600 K (10 per cent) hotter for this isochrone. In fact, this problem is known as the 'radius discrepancy', which is encountered especially in late-type dwarfs and has been a subject of debate for nearly half a century (see Southworth 2022).

These conflicting results were checked using the Granada (e.g. Claret 2006) and Padova (e.g. Bressan et al. 2012) evolutionary models, and similar results were obtained. On the other hand, it is obvious that it is not ideal to use standard single-star evolution models when studying the evolution of binary stars. Here, whereas the ellipticity effect (tidal-rotational deformations) and the reflection effect (from radiative interaction) – known as proximity effects between the components of binary stars – become important (Kopal 1959), mass transfer between components (due to a stellar wind and/or directly from a component filling its Roche lobe) plays an important role (e.g. Hurley et al. 2002). Stars in the 1.1–1.5 $M_\odot$ mass range, such as the primary component of SY Phe, are subject to the combined effects of core overshooting and He diffusion, whereas low-mass stars (below 1 $M_\odot$), such as the secondary component of

[2]https://www.unige.ch/sciences/astro/evolution/en/database/

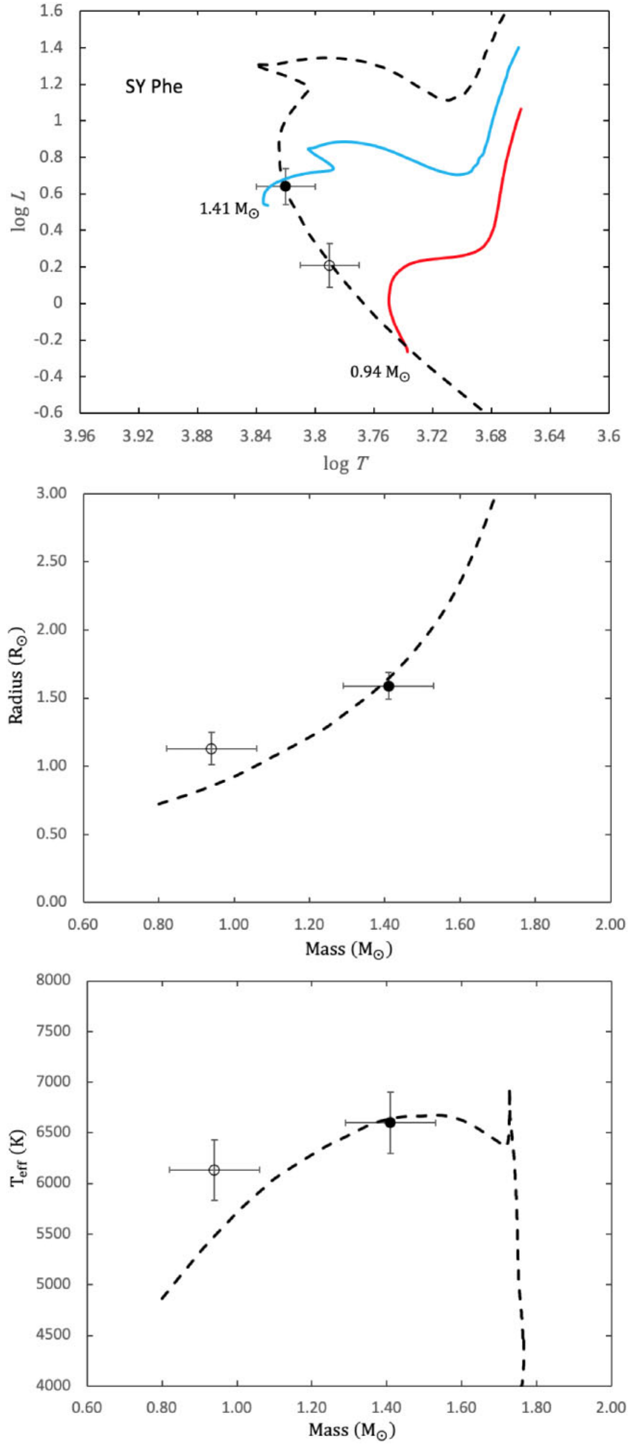

Figure 12. Location of the components of SY Phe in the H–R diagram (top panel), mass versus radius diagram (middle panel) and mass versus temperature diagram (bottom panel). The Geneva evolutionary tracks for 1.41 $M_\odot$ (blue line) and 0.94 $M_\odot$ (red line), corresponding to the primary and secondary stars, are plotted for $Z_\odot = 0.014$ in the H–R diagram. The Geneva isochrone of 2 Gyr for $Z = 0.014$ is also indicated by the dashed black curve. In all diagrams, filled and open circle symbols represent primary and secondary components, respectively. Vertical and horizontal lines show error bars of the measured quantities.

SY Phe, are subject to magnetic activity. These complications cause difficulties in the determination of ages of binary stars such as the SY Phe system (Torres et al. 2010).

The spectral type of the primary component and the effective temperatures of both components of SY Phe (see Section 4) indicate that these stars should have convective envelopes. In this case, using equation (6.2) in Zahn (1977) for stars with convective envelopes and the corresponding absolute parameters in Table 6 (above), the circularization time-scale was calculated as $\tau_{\rm circ} \approx 8 \times 10^9$ yr. On the other hand, the age of SY Phe was estimated at 2 Gyr. Therefore, if these two time-scales are compared, and considering that the orbit of SY Phe is still eccentric ($e \sim 0.007$), the observational findings for this system are in clear agreement with Zahn (1977)'s theory of circularization.

9 SUMMARY

In this study, SAAO mid-resolution spectroscopic and high-sensitivity *TESS* photometric observations of the eccentric EB star SY Phe were analysed for the first time. The results and problems encountered are summarized as follows:

(i) Through resolution of the RV and *TESS* light curves of SY Phe, the orbital and physical parameters of the binary system were calculated. Uncertainties of the order of 10 per cent remain because of the large amount of scatter in the RV curves.

(ii) Through a frequency analysis of *TESS* photometric observations, it was discovered that SY Phe displays a strong γ Dor pulsation mode, assigned to the primary component of the system.

(iii) The apsidal motion parameters of SY Phe were estimated from eclipse time variations spanning approximately 60 yr. Whereas the photometric observations serve to set a lower limit of 700 yr for the apsidal motion period (because of the large scattering in the data before 2015 in the $O - C$ diagram), when the high rotational velocity of the primary component is taken into account, the theoretical internal structure constant derived from Granada models (Claret 2006) suggests an apsidal motion period that is approximately twice as large as that obtained from the $O - C$ diagram.

(iv) The positions of the components of SY Phe in the H–R diagram indicate that the evolutionary age of the system is 2 Gyr. Here, it should not be overlooked that this 2 Gyr age is an estimate since the proximity effects and possibility of mass transfer between the components are not taken into account in the age determination of SY Phe. Moreover, the comparison of the observational findings and theoretical evolution models indicate that the radius and temperature of the secondary component, derived from the observations, is approximately 0.25 $R_\odot$ larger and 600 K hotter than the values predicted from the theoretical models.

ACKNOWLEDGEMENTS

This research was supported by TÜBİTAK (Scientific and Technological Research Council of Türkiye) under grant no. 121F203. CAE thanks the South African National Research Foundation and the University of Johannesburg for financial support. All the authors thank the SAAO for observing time. We also thank the unnamed referee for informative and helpful comments.

It is a pleasure to express our appreciation of the high quality and ready availability, via the Mikulski Archive for Space Telescopes (MAST), of data collected by the *TESS* mission. Funding for the *TESS* mission is provided by the NASA Explorer Program. The authors thank the ASAS, APPLAUSE, HIPPARCOS, KELT, Pi of the sky, SWASP and *TESS* teams for making all of the observations readily accessible on public platforms. This work made partial use of data from the European Space Agency (ESA) mission *Gaia* (https://www.cosmos.esa.int/gaia), processed by the *Gaia* Data Processing and Analysis Consortium (DPAC, https://www.cosmos.esa.int/web/gaia/dpac/consortium). Funding for the DPAC has been provided by national institutions, in particular, the institutions participating in the *Gaia* Multilateral Agreement. This research partly made use of the SIMBAD data base, operated at CDS, Strasbourg, France, and of NASA's Astrophysics Data System Bibliographic Services.

DATA AVAILABILITY

The majority of data included in this article are available as listed in the paper. The *TESS* data are available online from the MAST repository (https://mast.stsci.edu/portal/Mashup/Clients/Mast/Portal.html).

REFERENCES

Abbott T. M. C. et al., 2021, ApJS, 255, 20
Aerts C., Mathias P., Van Hoolst T., De Mey K., Sterken C., Gillet D., 1995, A&A, 301, 781
Bakış V., Eker Z., 2022, Acta Astron., 72, 195
Bevington P. R., 1969, Data reduction and error analysis for the physical sciences. McGraw-Hill, New York
Bressan A., Marigo P., Girardi L., Salasnich B., Dal Cero C., Rubele S., Nanni A., 2012, MNRAS, 427, 127
Budding E., Demircan O., 2007, An Introduction to Astronomical Photometry, 2nd edn. Cambridge Univ. Press, Cambridge, p. 434
Castelli F., Kurucz R. L., 2003, Proc. IAU Symp. 210, Modelling of Stellar Atmospheres. Astron. Soc. Pac., San Francisco, p. A20
Claret A., 2006, A&A, 453, 769
Claret A., 2017, A&A, 600, 30
Crause L. A. et al., 2016, in J. Evans, L. Simard, H. Takami, eds., Proceedings of the SPIE. Vol. 9908, SPIE Digital Library, id. 990827
Crause L. A. et al., 2019, J. Astron. Telesc. Instrum. Sys., 5, 024007
Ekström S. et al., 2012, A&A, 537, A146
Fabricius C., Høg E., Makarov V. V., Mason B. D., Wycoff G. L., Urban S. E., 2002, A&A, 384, 180
Fokin A., Mathias P., Chapellier E., Gillet D., Nardetto N., 2004, A&A, 426, 687
Gaia Collaboration, 2023, A&A, 674, 22
Gaia Collaboration, 2018, A&A, 616, A1
Gray R. O., Corbally C. J., 2008, Stellar Spectral Classification. Princeton Univ. Press, Princeton
Groote D., Tuvikene T., Edelmann H., Arlt R., Heber U., Enke H., 2014, Astroplate 2014. Inst. Chem. Technol., Prague, p. 53
Hadrava P., 1995, A&AS, 114, 393
Hoffmeister C., 1949, AAAN, 12, 23
Hoffmeister C., 1958, Veroeffentlichungen der Sternwarte Sonneberg, 3, 333
Houk N., 1978, Michigan catalogue of two-dimensional spectral types for the HD stars. Vol. 2, Ann Arbor: Dept. Astron., Univ. Michigan
Hurley J. R., Tout C. A., Pols O. R., 2002, MNRAS, 329, 897
Jenkins J. M. et al., 2016, Proc. SPIE Conf. Ser. Vol. 9913, Software and Cyberinfrastructure for Astronomy IV. SPIE, Bellingham, p. 99133E
Kim C.-H., Kreiner J. M., Zakrzewski B., Ogłoza W., Kim H.-W., Jeong M.-J., 2018, ApJS, 235, 41
Kopal Z., 1959, Close Binary Systems. Chapman & Hall, London
Lenz P., Breger M., 2004, Proc. IAU 2004, AUS224, 786
Lucy L. B., 1967, Z. Astrophysik, 65, 89
Maceroni C. et al., 2014, A&A, 563, A59
Maceroni C., Montalbán J., Gandolfi D., Pavlovski K., Rainer M., 2013, A&A, 552, A60
Mason B. D., Wycoff G. L., Hartkopf W. I., Douglass G. G., Worley C. E., 2001, AJ, 122, 3466
Maxted P. F. L. et al., 2020, MNRAS, 498, 332
McMahon R. G., Banerji M., Gonzalez E., Koposov S. E., Bejar V. J., Lodieu N., Rebolo R., the VHS collaboration, 2013, The Messenger, 154, 35
Mowlavi N. et al., 2023, A&A, 674, A16
Oelkers R. J. et al., 2018, AJ, 155, 39
Overall S., Southworth J., 2024, accepted for publication in The Observatory, 10.48550/arXiv.2401.13397
Pecaut M. J., Mamajek E. E., 2013, ApJS, 208, 9
Pepper J. et al., 2007, PASP, 119, 923
Pollacco D. L. et al., 2006, PASP, 118, 1407
Popper D. M., Jeong Y.-C., 1994, PASP, 106, 189
Ruciński S. M., 1969, Acta Astron., 19, 245
Skrutskie M. F. et al., 2006, AJ, 131, 1163
Southworth J., 2013, A&A, 557, 119
Southworth J., 2022, The Observatory, 142, 267
Southworth J., 2023, The Observatory, 143, 71
Southworth J., Clausen J. V., 2007, A&A, 461, 1077
Spencer J. H., Jackson J., 1936, Proper Motions of Stars in the Zone Catalogue –40 to –52 degrees of 20843 Stars for 1900, Her Majesty's Stationary Office (HMSO), London
Tokovinin A., 2018, ApJS, 235, 6
Tonry J., Davis M., 1979, AJ, 84, 1511
Torres G., Andersen J., Giménez A., 2010, A&AR, 18, 67
Wenger M. et al., 2000, A&AS, 143, 9
Wilson R. E., Devinney E. J., 1971, ApJ, 166, 605
Yusof N. et al., 2022, MNRAS, 511, 2814
Zahn J.-P., 1977, A&A, 57, 383
Zasche P., 2012, New Astron., 17, 687
Zola S., Rucinski S. M., Baran A., Ogloza W., Pych W., Kreiner J. M., 2004, Acta Astron., 54, 299

APPENDIX A: TABLE OF RADIAL VELOCITY MEASUREMENTS

Table A1. RV measurements of the components of SY Phe. The values in the $O-C$ columns represent the deviations of the individual measurements from the fitted RV curves.

No	Time (HJD-2450000)	RV_1 (km s^{-1})	$(O-C)_1$ (km s^{-1})	RV_2 (km s^{-1})	$(O-C)_2$ (km s^{-1})
1	58815.4627	53.56	8.44	−68.61	16.54
2	58815.4761	49.55	3.69	−69.71	13.51
3	58817.3502	23.45	14.69	−14.66	−8.28
4	58817.3620	2.09	−5.77	−13.32	−9.91
5	58817.3737	−15.49	−22.45	−11.99	−7.51
6	58817.3861	10.73	4.72	−10.58	−1.10
7	58817.3985	7.76	2.70	−9.16	−2.59
8	58819.3186	−47.75	5.09	76.77	14.53
9	58819.3342	−48.85	3.24	75.66	7.31
10	58819.3494	−48.13	3.22	74.55	7.32
11	58819.3669	−39.51	10.96	73.25	6.58
12	58819.3819	−36.69	13.00	72.10	15.75
13	58819.3998	−44.76	3.99	70.70	7.69
14	58819.4163	−49.24	−1.38	69.38	5.26
15	58820.3321	24.87	6.48	−28.94	−13.07
16	58820.3477	18.11	−1.44	−30.67	16.06
17	58820.3630	18.43	−2.26	−32.36	4.43
18	58820.3817	4.73	−17.34	−34.40	−47.76
19	58820.3970	36.58	13.39	−36.06	−4.70
20	58821.3139	71.56	7.12	−97.29	1.81
21	58821.3293	74.58	10.02	−97.47	6.74
22	58821.3443	66.77	2.12	−97.61	8.46
23	58821.3601	66.91	2.18	−97.73	8.37
24	58821.3752	59.65	−5.14	−97.81	2.39
25	58821.3905	65.16	0.34	−97.86	−0.90
26	58822.3068	39.34	7.80	−48.47	15.08
27	58822.3205	37.79	7.17	−47.10	7.17
28	58822.3359	39.48	9.90	−45.55	10.20
29	58822.3521	45.93	17.47	−43.90	0.51
30	58822.3673	28.38	0.97	−42.34	18.88
31	58822.3831	21.70	−4.61	−40.70	−6.60
32	58823.3274	−45.88	−3.50	61.25	−0.82
33	58823.3410	−39.44	3.75	62.45	7.11
34	58823.3561	−42.67	1.41	63.76	0.91
35	58823.3712	−43.58	1.37	65.05	1.00
36	58823.3864	−44.47	1.34	66.33	1.08
37	58824.3861	−80.21	−19.41	88.59	−24.25
38	58824.4016	−85.99	−25.67	87.87	−25.06
39	58825.3051	−5.89	−1.17	5.35	−14.01
40	58825.3203	7.10	10.63	3.58	−21.06
41	59214.3104	−53.69	10.16	93.11	9.81
42	59214.3238	−77.06	−13.48	92.71	5.14
43	59216.3327	39.86	−18.11	−87.68	−11.45
44	59216.3481	36.88	−21.61	−88.46	−5.30
45	59216.3632	55.87	−3.11	−89.19	−3.18
46	59217.3201	56.13	6.71	−75.00	7.28
47	59217.3353	33.12	−15.54	−73.87	−13.76
48	59217.3506	35.77	−12.11	−72.71	−5.56

APPENDIX B: TABLE OF TIMES OF ECLIPSES

Table B1. Times of eclipses for SY Phe.

Time (HJD-2400000)	Error (d)	Type P/S	Source/ /Reference
58358.90410	0.00082	P	*TESS*
58361.52068	0.00010	S	*TESS*
58364.17424	0.00054	P	*TESS*
58366.79132	0.00005	S	*TESS*
58369.44458	0.00012	P	*TESS*
58372.06145	0.00010	S	*TESS*
58374.71676	0.00008	P	*TESS*
58377.33180	0.00013	S	*TESS*
58379.98839	0.00021	P	*TESS*
58382.60393	0.00080	S	*TESS*
58385.25792	0.00009	P	*TESS*
58387.87406	0.00039	S	*TESS*
58390.52899	0.00010	P	*TESS*
58393.14515	0.00101	S	*TESS*
58395.79975	0.00007	P	*TESS*
58398.41485	0.00067	S	*TESS*
58401.07018	0.00058	P	*TESS*
58403.68623	0.00026	S	*TESS*
58406.34000	0.00001	P	*TESS*
58408.95813	0.00011	S	*TESS*
59091.55724	0.00037	P	*TESS*
59094.17328	0.00079	S	*TESS*
59096.82774	0.00078	P	*TESS*
59099.44501	0.00052	S	*TESS*
59096.82774	0.00078	P	*TESS*
59104.71539	0.00106	S	*TESS*
59107.37151	0.00079	P	*TESS*
59109.98707	0.00079	S	*TESS*
59112.64059	0.00158	P	*TESS*
59115.25712	0.00010	S	*TESS*
59117.91196	0.00020	P	*TESS*
59120.52785	0.00057	S	*TESS*
59123.18278	0.00105	P	*TESS*
59125.79869	0.00008	S	*TESS*
59123.18278	0.00105	P	*TESS*
59131.06963	0.00046	S	*TESS*
59133.72512	0.00132	P	*TESS*
59136.34022	0.00105	S	*TESS*
59138.99637	0.00079	P	*TESS*
59141.61197	0.00105	S	*TESS*
60187.90099	0.00141	S	*TESS*
60190.51810	0.00100	S	*TESS*
60193.17395	0.00112	P	*TESS*
60195.78850	0.00053	S	*TESS*
60198.44617	0.00121	P	*TESS*
60201.06014	0.00094	S	*TESS*
60203.71544	0.00078	P	*TESS*
60206.33269	0.00103	S	*TESS*
55860.50751	0.00083	P	KELT
55863.11637	0.00081	S	KELT
56224.19695	0.00079	P	KELT
56226.80835	0.00023	S	KELT
56587.88383	0.00060	P	KELT
56590.50350	0.00052	S	KELT
55459.91649	0.00636	P	KELT
55462.53189	0.00258	S	KELT
55807.79434	0.00087	P	KELT
55810.41302	0.00061	S	KELT
56171.48736	0.00121	P	KELT
56174.10049	0.00221	S	KELT
56535.17327	0.00145	P	KELT
56537.79118	0.00048	S	KELT
52286.84154	0.00209	P	ASAS
52289.45565	0.00071	S	ASAS
53024.75623	0.00289	P	ASAS
53027.37914	0.00001	S	ASAS
53731.06143	0.00052	P	ASAS
53733.67711	0.00116	S	ASAS
54395.19428	0.00308	P	ASAS
54827.40388	0.00250	P	ASAS
53704.70928	0.00260	P	Pi of the sky
53707.32031	0.00474	S	Pi of the sky
54421.54653	0.00053	P	Pi of the sky
54735.14852	0.00237	S	Pi of the sky
48465.44435	0.00272	P	*HIPPARCOS*
48468.05847	0.00500	S	*HIPPARCOS*
53902.34769	0.00112	S	SWASP
53941.89659	0.00077	P	SWASP
53955.05454	0.00100	S	SWASP
53981.40958	0.00009	S	SWASP
53989.33983	0.00290	P	SWASP
54007.76167	0.00105	S	SWASP
54031.50085	0.00106	P	SWASP
54047.31716	0.00115	P	SWASP
54297.66679	0.00132	S	SWASP
54334.55438	0.00131	S	SWASP
54347.75612	0.00070	P	SWASP
54363.56726	0.00032	P	SWASP
54384.65170	0.00117	P	SWASP
54387.26516	0.00345	S	SWASP
54411.00902	0.00085	P	SWASP
54413.62019	0.00273	S	SWASP
54426.81399	0.00079	P	SWASP
54429.43696	0.00184	S	SWASP
54437.36061	0.00133	P	SWASP
54445.24526	0.00105	S	SWASP
39942.40580	0.00517	P	APPLAUSE
39945.01813	0.00703	S	APPLAUSE

This paper has been typeset from a TEX/LATEX file prepared by the author.